Article

Pre- and Post-Liquefaction Behaviors of Manufactured Sand Considering the Particle Shape and Stress History Effects

Zhe Wang [1,2,3], **Guanyu Chen** [2], **Dazhi Wu** [2,*], **Yao Li** [4] **and Juntao Hu** [2]

1. Department of Civil Engineering, Faculty of Engineering, Lishui University, Lishui 323000, China
2. School of Civil Engineering and Architecture, Zhejiang Sci-Tech University, Hangzhou 310018, China
3. College of information Engineering, Zhejiang University of Technology, Hangzhou 310023, China
4. School of Highway, Chang'an University, Xi'an 710064, China
* Correspondence: wudz@zstu.edu.cn

Abstract: As the substitution of natural quartz sand (QS), manufactured sand (MS) is highly demanded in the filling and reclamation of foundations in geotechnical engineering, which may be subjected to cyclic shear stresses induced by wave, seismic, and traffic loadings. One of the noticeable distinctions between MS and QS is their particle shape, which has a significant effect on their shear and liquefaction behaviors under the monotonic and cyclic shear stresses, and needs to be further investigated. In this study, the particle shapes of MS and QS were quantitatively characterized by metallurgical microscope tests and digital image processing. Their pre- and post-liquefaction behaviors were evaluated by a series of direct shear tests, cyclic simple shear tests (CSS), and post-liquefaction monotonic shear tests (PMS). The results show that in the CSS test, samples with irregular particles showed stronger liquefaction and shear resistances, indicating that MS was more stable under cyclic shear loadings. In the PMS tests, it was found that the liquefaction and shear resistances of the samples not only increased with the increasing particle irregularity but also with the increasing shear amplitude in the pre-liquefaction stage. Furthermore, quantitative relationships between the particle shape, shear history, and indexes of shear and liquefaction behaviors of the samples were proposed by regression analysis. The research findings could guide the application of MS in offshore and foundation engineering and provide a reference for the selection of MS and its foundation design.

Keywords: manufactured sand; pre- and post-liquefaction; particle shape; stress history; cyclic simple shear

1. Introduction

Manufactured sand (MS) is produced from crushed and screened rocks. In recent years, MS has been widely used for infrastructure projects, which not only reflects the shortage of natural sand resources, but also shows a promising market and greener nature of MS in the future [1–3]. In geotechnical engineering, MS is greatly demanded as the substitution of natural quartz sand (QS) for the filling and reclamation layer during the construction of subgrade, artificial islands, airport runways, embankments, retaining walls, etc. [4]. For instance, it is reported that the reclamation of Jiaoyi Island needs hundreds of millions of tons of MS [5]. Compared with natural sand, the particle shape, gradation, and stone powder content of MS show a significant difference, which leads to different engineering properties as well [6–9].

The particle shapes of MS are various due to differences in the parent rock and crushing equipment. According to several studies, the particle morphology of granular materials has a significant impact on their mechanical responses [10–13]. Yang and Luo [14] stated that the shape of particles could be a more important factor than their grading. Yang and Wei [15] also observed that particle shape, rather than particle stiffness, had a greater impact on shear properties. The friction angle of granular materials was also found to

be highly related to the particle angularity [16]. Moreover, it was observed that particle geometry has a greater impact on its mechanical behaviors than roughness [17]. These findings suggest that the particle shape has a major impact on shear behaviors of granular materials including MS. Therefore, it is crucial to strengthen the mechanical response by selecting the appropriate particle shape of MS.

Meanwhile, as saturated sand foundation is susceptible to liquefaction and deformation under dynamic loadings such as seismic and wave loadings, it is critical to assess the dynamic properties of MS for the safety of foundation engineering. Moreover, the impact of gravity and other static lateral stress in the foundation could also generate large deformation and cause liquefaction again after the initial liquefaction happened, bringing a potential safety hazard to the structures, including seabed, retaining walls, and embankments [18,19], as this static stress induced post-liquefaction is hard to predict and often causes sudden failure of the foundation. Liquefaction occurs when the pore water pressure of saturated sand reaches the effective stress under cyclic loadings, as the sand has lost its bearing capacity, and comes to a flow state [20–24]. Many variables, including relative density, strain amplitude, and cyclic numbers, have been identified to influence the liquefaction response in previous researches [25–30]. In early studies, to enhance the liquefaction resistance of soils, some unusual backfilling materials, such as tire-derived aggregates and recycled glass, were tested to assess their behaviors under dynamic loadings [31–33]. Mckelvey et al. [34] and Li et al. [35] tested recycled concrete aggregate (RCA) in a variety of direct shear and triaxial tests, proving their promising potential as backfilling materials. The mechanical properties of RCA, which can be regarded as a type of MS, have been analyzed in previous studies which found that it can be utilized for pavement bases and road backfilling [36–40]. However, few researches have quantitatively assessed the particle shape and studied the effect of the particle shape on the liquefaction behaviors of these angular materials, especially the MS that is crushed from rocks. The pre- and post-liquefaction behaviors, as well as the relationship between particle shape characteristics and responses under cyclic and monotonic shearing of MS, need to be further investigated.

This paper aims to study the effects of particle shape and shear history on pre- and post-liquefaction behaviors of MS and compare the particle geometry and shear behaviors of QS and MS. A series of cyclic simple shear (CSS) and post-liquefaction monotonic shear (PMS) tests was used to investigate the effect of particle shape and stress history on their pre- and post-liquefaction behaviors. The relationships between the particle shape, cyclic shear amplitude, and shear performance were revealed. The shear stiffness, damping ratio, volumetric strain, shear strength, and pore pressure of MS were also examined to offer a basic understanding of the mechanical behaviors of MS, which could support the application of MS in geotechnical engineering.

2. Materials and Methods

Four kinds of MS widely used in Zhejiang province, China, were used in this study. They were manufactured sand created from basalt (MSB), sandstone (MSS), sandstone with rhyolitic crystal tuff (MSSR), and river pebble (MSR). Compared with MS, there is inapparent difference of particle shape between different kinds of natural QS because of the nature of their relatively rounder and more regular particle shapes. Therefore, Leighton Buzzard sand fraction B (LBS), which is a kind of natural quartz sand as well as a standard sand widely used in geotechnical tests from UK, was chosen as the representative natural QS and used in the control group to comparatively investigate the effect of particle shape and demonstrate the features of shear behaviors of MS. In the experimental tests, for controlling variables, samples were screened and classified to identical gradation and particle size, and ASTM standards D4253 [41] and D4254 [42] were adopted to obtain their maximum and minimum void ratios. Their particle distribution and physical parameters are presented in Figure 1 and Table 1. Their internal friction angles, which are shown in Figure 2, were obtained by direct shear tests. The friction angles (φ) of samples for LBS, MSSR, MSB, MSS, and MSR were 32.5°, 40.6°, 43.4°, 43.8°, and 45.6°, respectively.

In general, MS samples have higher friction angles than QS because the irregular shapes of MS samples can restrain the dislocation between particles, as the particles around the interface have to climb over the adjacent particles before they can move under the shearing.
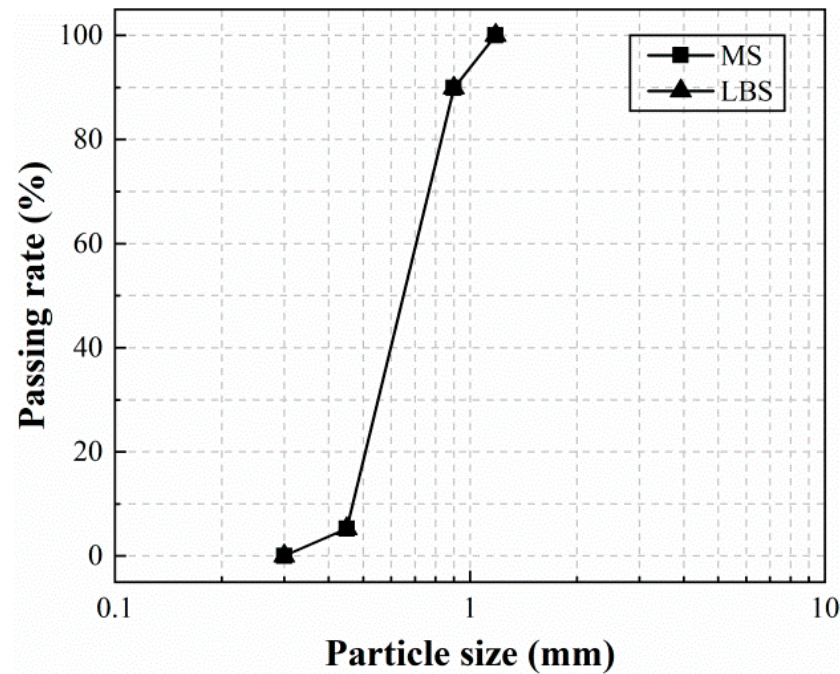

Figure 1. Particle size distribution of samples.

Table 1. Physical properties of samples.

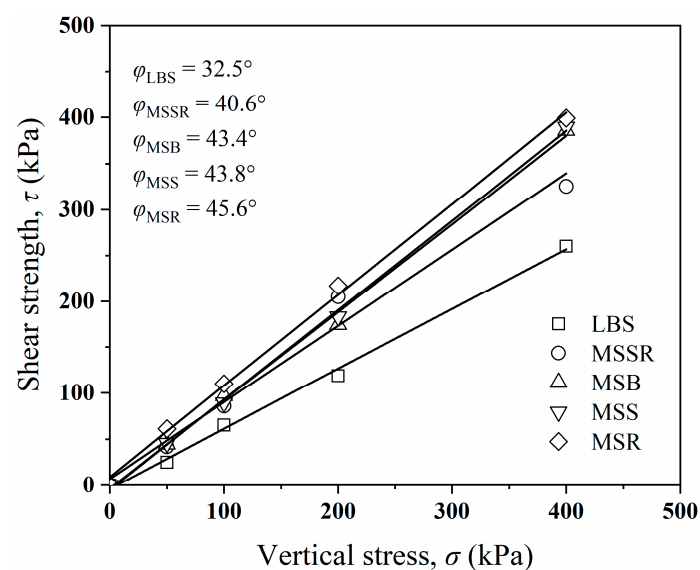| Material	LBS	MSSR	MSB	MSS	MSR
Specific gravity G_s (g/cm^3)	2.65	2.65	2.65	2.60	2.70
Maximum void ratio e_{max}	0.79	1.023	0.992	1.016	1.09
Minimum void ratio e_{min}	0.52	0.606	0.589	0.585	0.636
Uniformity mean diameter D_{50} (mm)	0.62	0.62	0.62	0.62	0.62

Figure 2. Friction angle of samples.

2.1. Particle Shape Evaluation

The morphology parameters of samples were evaluated by particle roundness, sphericity, and regularity, which was first proposed by Wadell [43]. After that, Krumbein [44] proposed an image processing method to calculate the parameters and improvements have been made by several researchers [45–47]. The particle sphericity, roundness and regularity are defined as follows [48–50]:

Sphericity (*S*):

$$S = \frac{D_{max-insc}}{D_{min-insc}};$$
(1)

roundness (*R*):

$$R = \frac{\sum D_c}{N_c \cdot D_{max}};$$
(2)

and regularity (*ρ*):

$$\rho = \frac{S + R}{2},$$
(3)

where $D_{max-insc}$ is the particle's maximum inscribe cycle diameter, $D_{min-circ}$ is the minimum diameter of the circumcircle, D_c and N_c are the diameter and number of other cycles except the largest in-circle, respectively, and D_{max} is the largest inscribed corner cycle.

For each group, 1000 particles were chosen randomly and photographed with a microscope. The photos were then binarized by the Image-Pro-Plus software. Figure 3a–e show the binary pictures of the particle shape and they were imported to Python for calculation. Figure 4 presents the cumulative distribution curves of the testing materials. For a given sample, the values corresponding to the 50% of the cumulative distribution are defined as the representative shape parameters. The calculated results of sphericity, roundness, and regularity of the samples are described in Table 2. The particle regularity (*ρ*) was used to characterize the particle geometries as a major particle shape factor. The results showed that the sphericity and roundness of LBS are higher than those of MS, indicating that their particles are rounder and more regular. As a representative parameter of particle shape, the regularity (*ρ*) of samples for LBS, MSSR, MSB, MSS, and MSR were 0.803, 0.607, 0.536, 0.498, and 0.432, respectively, which also proved that the particles of MS are more angular. The relationship between the maximum void ratio, minimum void ratio, and particle regularity are shown in Figure 5. It can be seen that the maximum and minimum void ratio could be significantly influenced by the particle shape. The maximum and minimum void ratio, as well as the difference between them, tend to decrease with increasing particle regularity, similar to the conclusion from Zheng et al. [51].
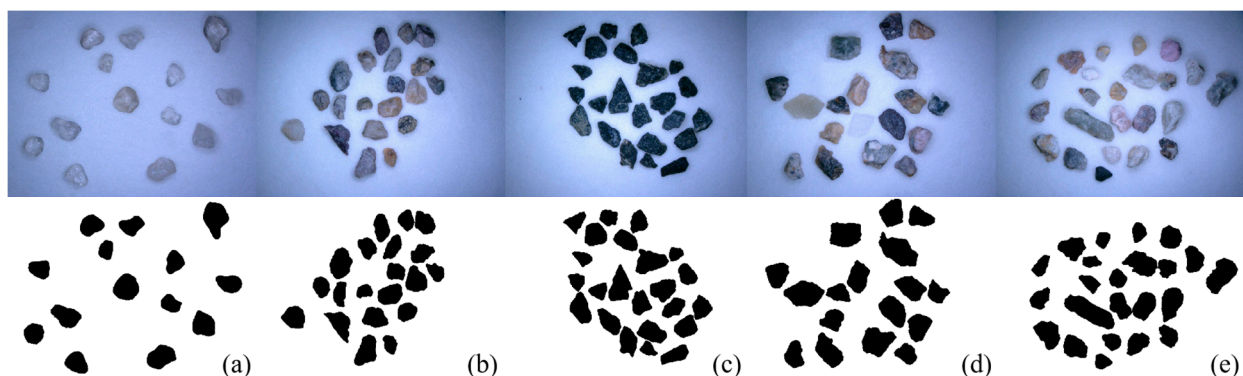
Figure 3. Binary images of the particle shapes of: (**a**) LBS; (**b**) MSSR; (**c**) MSB; (**d**) MSS; and (**e**) MSR.
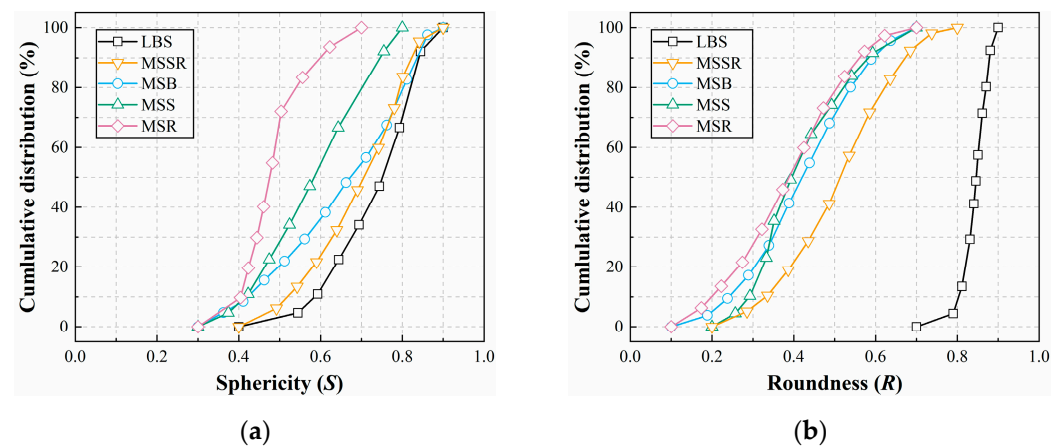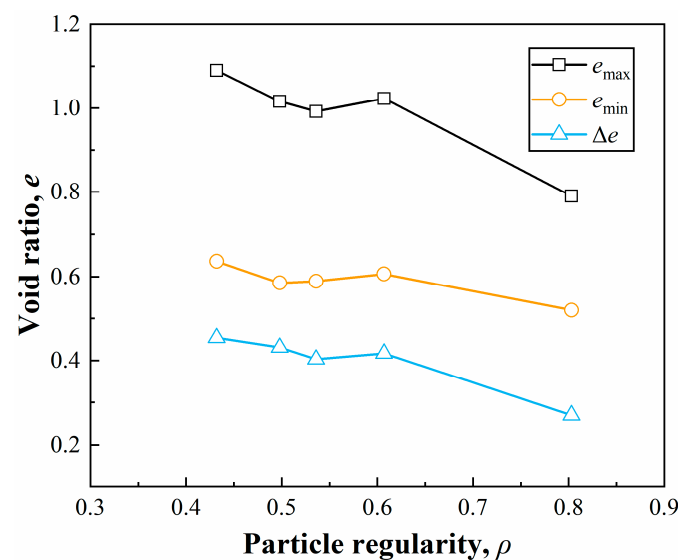
Figure 4. Cumulative distribution curves of the shape parameters of the samples: (**a**) sphericity and (**b**) roundness.

Table 2. Average values of sphericity, roundness, and regularity of samples.

| Material	Sphericity (S)	Roundness (R)	Regularity (ρ)
LBS	0.76	0.846	0.803
MSSR	0.702	0.512	0.607
MSB	0.651	0.421	0.536
MSS	0.604	0.392	0.498
MSR	0.478	0.386	0.432

Figure 5. Relationship between the void ratio and particle regularity of the testing materials.

2.2. Relationships between the Particle Shape and Friction Angle

Combining the results of friction angles in Figure 2 and the corresponding particle regularity in Table 2, Figure 6 depicts an analysis of the relationship between the particle regularity and friction angle. Generally, the friction angle and particle regularity of samples show a linear correlation. In the range 0.432–0.803, the interface friction angle clearly decreases with the increasing particle regularity, demonstrating that particle interlocking was stronger with irregular shapes. The connection between the friction angle and particle regularity can be expressed as Equation (4):

$$\varphi = -36.066\rho + 61.925 \tag{4}$$
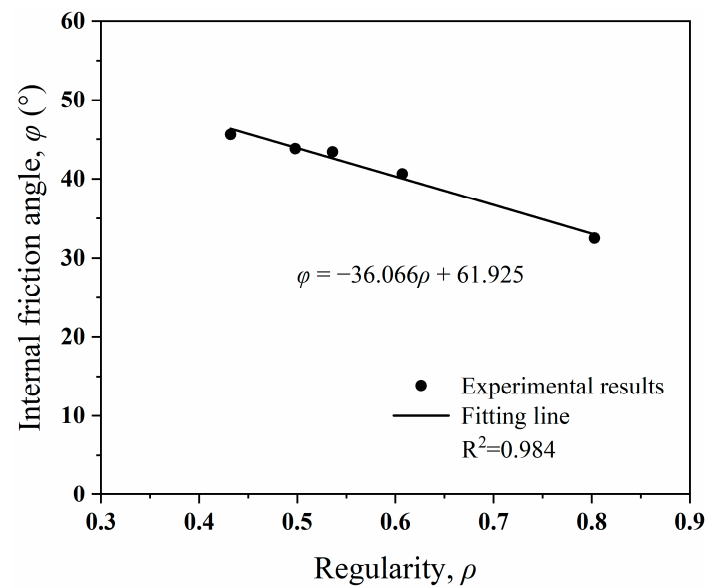
Figure 6. Relationship between the particle regularity and friction angle.

Therefore, the particle regularity is a significant factor for MS and QS as different particle regularities could contribute to the different mechanical behaviors of the sand.

## 3. Experimental Apparatus and Methods

The pre- and post-liquefaction behaviors of MS under cyclic and monotonic shear were investigated using an electro-mechanical dynamic cyclic simple shear system (EMDCSS), shown in Figure 7. The device can provide a vertical direction and a horizontal direction shear loading. The samples were placed in a cylindrical opening that measured 30 mm in height and 50 mm in diameter and was encircled by a stack of low friction rings. The influence of particle regularity (0.432–0.803) and shear strain amplitude (0.1%, 0.2%, 0.3%, and 0.4%) on the shear behaviors of the samples was investigated by CSS and PMS tests, following the testing guidelines proposed in ASTM D8296-19 [52].
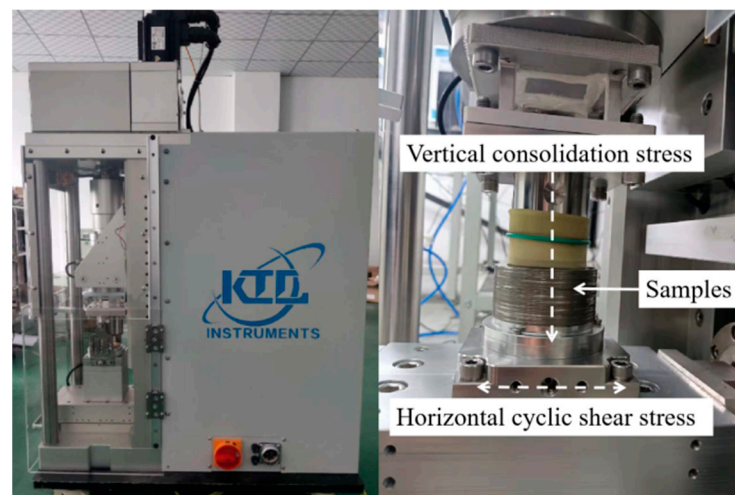
Figure 7. Cyclic simple shear apparatus.

A dry funnel was used to fill the cylinder shear box with oven-dried samples of predefined weights. Samples with a relative density of 46%, which can be defined as medium dense sand [53,54], were adopted to better conduct the comparative study of the liquefaction behavior because of their relatively larger liquefaction tendency. Initially, a K_0 consolidation was imposed with the effective vertical stress σ_v of 50 kPa for 30 min,

which was identified as the first consolidation. A strain-controlled undrained CSS test was then carried out with a cyclic number of 250 and several cyclic shear strain amplitudes. Figure 8 depicts the cyclic loading waveform in one cycle of the CSS tests and the loading frequency was set to be 0.1 Hz, which applies to the continued wave loading condition [55]. The vertical displacement was maintained to keep the volume unchanged. The initial liquefaction was considered to occur when the loss of vertical stress reached 95% as in the cyclic shear condition, and the change in vertical stress in dry sand is equivalent to the true water pressure in saturated sand [56].
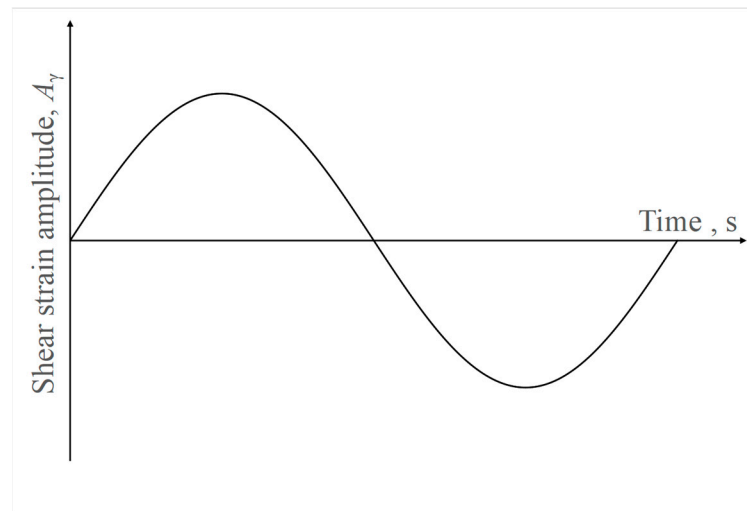
Figure 8. Loading waveform of the cyclic shear loading.

The liquefied samples were re-consolidated after the CSS tests were completed in the same condition of the first consolidation. Finally, the undrained PMS tests were conducted with the fixed vertical displacement as well. The horizontal displacement loading velocity was chosen at 0.05 mm/min to completely record the equivalent pore pressure development in post-liquefaction stage and the relationship between the shear strain and stress. Test conditions for samples are summarized in Table 3. Furthermore, samples without a history of liquefaction were evaluated under the same undrained monotonic shear condition to provide a reference.

Table 3. Test conditions for the samples.

	Pre-Liquefaction			Post-Liquefaction	
Testing No.	Consolidation stress (σ_v, kPa)	Samples	Cyclic shear strain amplitude (A_γ, %)	Re-consolidation stress (σ_v, kPa)	Monotonic shear
1		LBS			
2		MSSR			
3	/	MSB	/	50	Along the x-direction
4		MSS			
5		MSR			
6–10		LBS			
11–15		MSSR			
16–20	50	MSB	0.1, 0.2, 0.3, 0.4	50	Along the x-direction
21–25		MSS			
25–30		MSR			

4. Results and Discussion

4.1. Pre-Liquefaction Behaviors

The shear stiffness not only served as the primary parameter of soil dynamics research, but is also an important basis for the seismic analysis and in-situ seismic safety performance evaluation. The definition of shear stiffness (*K*) is illustrated in Figure 9 and Equation (5).

$$K = \frac{\tau_{max} + \tau_{min}}{2 \cdot \Delta} \tag{5}$$
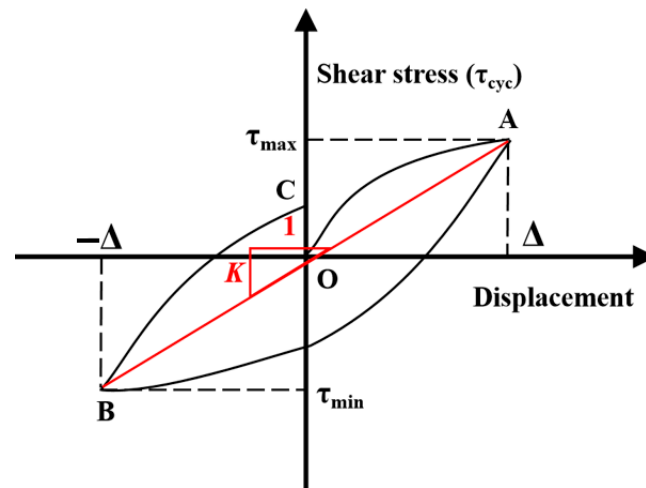

Figure 9. The definition of shear stiffness.

Figure 10 illustrates the variation of shear stiffness with cyclic number and shear strain amplitudes. It can be seen that for a certain shear amplitude, the shear stiffness decreased dramatically in the first 10 cycles as the shear stress reduced and the shear stress-strain hypothesis loops became flattened under cyclic shearing. As the cyclic loading continued to proceed, the decrease in shear stress became slower, as well as the shear stiffness. In general, the shear stiffness of the MS samples was greater than that of the LBS samples due to their irregular shapes, which enhanced the interlocking force of particles. In contrast, the particles of the LBS sample were more inclined to dislocate and rotate with smooth and regular shapes, leading to the quicker reduction of the shear stiffness as well as to a lower cyclic shear resistance in the first 10 cycles and the inapparent reduction of the shear stiffness in the later stage. Meanwhile, for a specific regularity and cyclic number, the shear stiffness with greater shear amplitude becomes smaller in the first tens of cycles. As the magnitude of the shear stress was approximately similar, the difference mainly comes from the effect of different shear strain amplitudes.
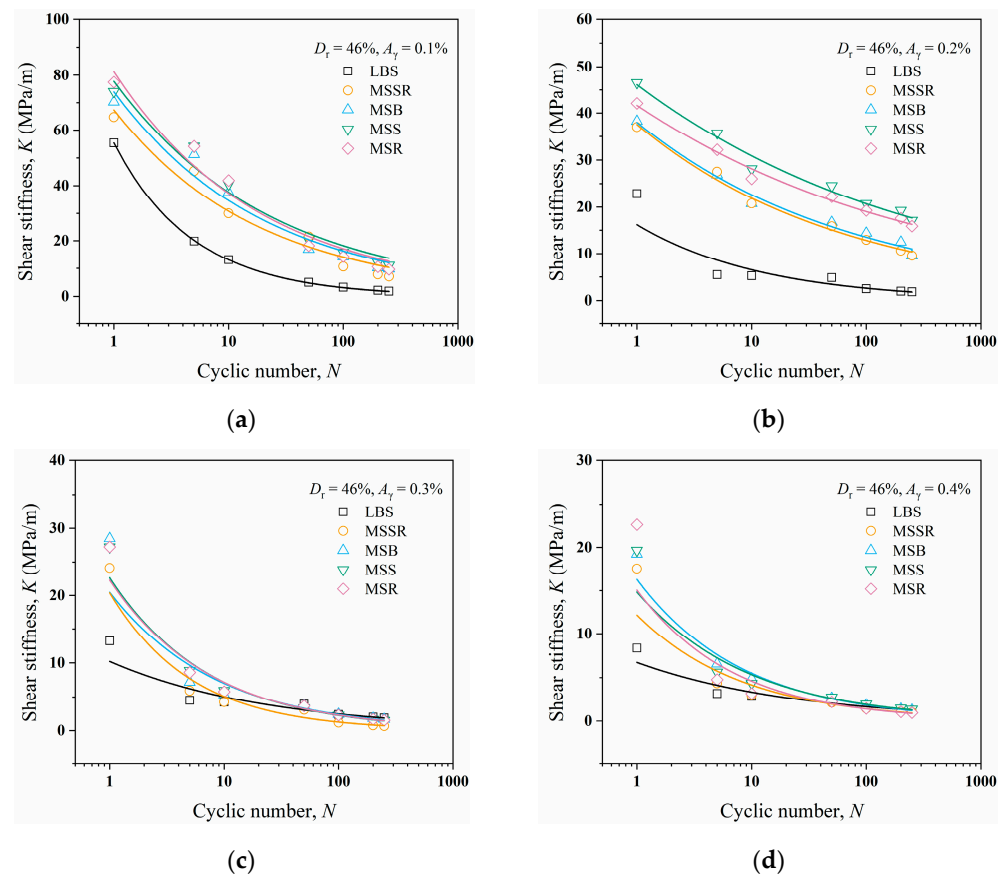
Figure 10. Shear stiffness of samples against the cyclic number with different cyclic shear strain amplitudes (σ_v = 50 kPa, D_r = 46%): (**a**) A_γ = 0.1%; (**b**) A_γ = 0.2%; (**c**) A_γ = 0.3%; and (**d**) A_γ = 0.4%.

4.1.1. Relationships between the Shear Stiffness, Particle Shape, and Cyclic Number

Based on the results in Figure 10, a power function is proposed to describe the changes of the shear stiffness with cyclic number, which can be described as:

$$K = A \cdot (N)^{-B} \tag{6}$$

where A and B are adaptation values of the equation, which depends on the particle regularity and shear strain amplitude. The coefficient A describes the mechanical properties of samples. A higher value of A represents more stable samples under the cyclic shear. The value of B represents the decreasing rate of the shear stiffness. A higher value of B indicates that the shear stiffness decreases more quickly with the same value of A.

Figure 11 summarizes the variations of these two parameters with the particle regularity under different shear amplitudes to further investigate the relationship between the shear stiffness and particle geometry. In Figure 11a, for a given shear strain amplitude, samples with lower regularity have higher A value, which means that irregular particles contribute to better shear performance under cyclic loadings. For a given regularity, the coefficient A decreases with an increasing shear strain amplitude, indicating that samples are more sensitive to liquefaction with higher cyclic shear amplitude. With a shear strain amplitude of 0.1%, the B value of LBS is larger than that of MS in Figure 11b, suggesting that the shear stiffness of LBS drops more quickly in this circumstance. The value B of MS samples, on the other hand, rose when the shear strain amplitude increased. This is because the initial shear stiffness of MS samples was higher than the LBS samples and the LBS sample liquefied rapidly in the first few cycles, resulting in the shear stiffness of LBS samples seldom decreasing in the later stage.
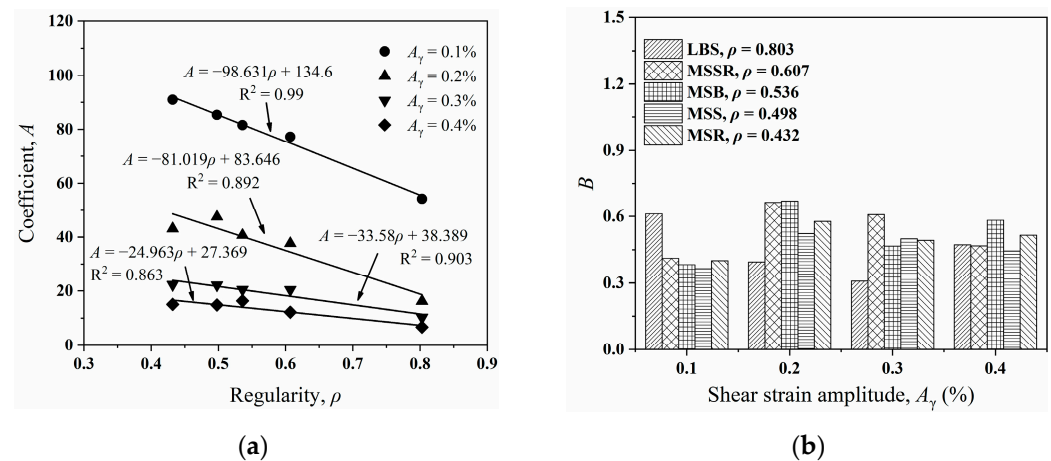
Figure 11. Variations of fitting parameters: (**a**) *A* value; (**b**) *B* value.

4.1.2. Liquefaction Resistance

Figure 12 presents the number of cycles required for the samples to reach liquefaction. The MS samples generally showed higher liquefaction resistance than the LBS samples because their higher irregularity restrains the overriding of the particles along the shear direction, as it is reported that the build-up of pore pressure in undrained cyclic loading conditions is caused by the continuing movement and rearrangement of sand particles, which leads to the densification and net amount of contraction of soil in each loading cycle upon loading reversal [57]. Figure 12 illustrates that the number of cycles to liquefy were also influenced by the shear strain amplitude. For a specified regularity, the cyclic number decreases with relatively higher shear strain amplitude, indicating that the larger vibrations accelerate the pore pressure generation of soils. Similar results were found in other studies [58,59], where the mechanical response of the sand materials was investigated.
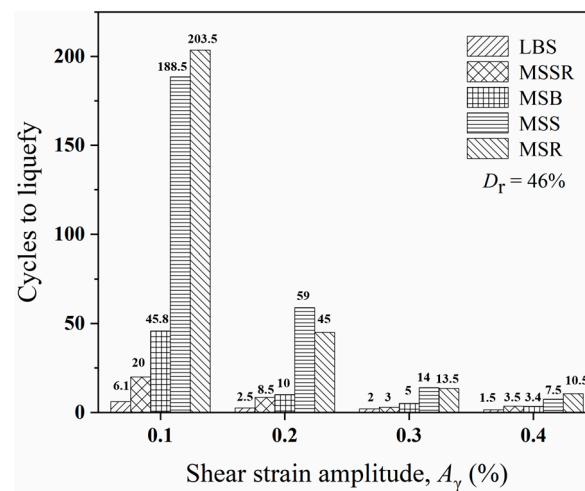

Figure 12. Liquefaction resistance of samples with different cyclic shear strain amplitudes.

4.2. Post-Liquefaction Behaviors

After the samples had experienced pre-liquefaction, a vertical stress was exerted to simulate the re-consolidation process induced by gravity. Figure 13 presents the volumetric strain developed during this stage. The results demonstrate that samples exhibited larger volumetric deformation in the re-consolidation stage with higher cyclic shear amplitude in the pre-liquefaction stage. This is because the higher loss of the vertical stress and larger amount of contraction induced by larger cyclic shear strain amplitude in the pre-liquefaction stage can lead to higher compressibility of samples in the re-consolidation stage. Furthermore, the difference of volumetric strains development between samples

tended to diminish as the shear amplitude increased. The results indicate that the amount of settlement of soil under its gravity after the dynamic loading, e.g., the wave loading, apparently depends on the amplitude of cyclic shearing in the early stage.
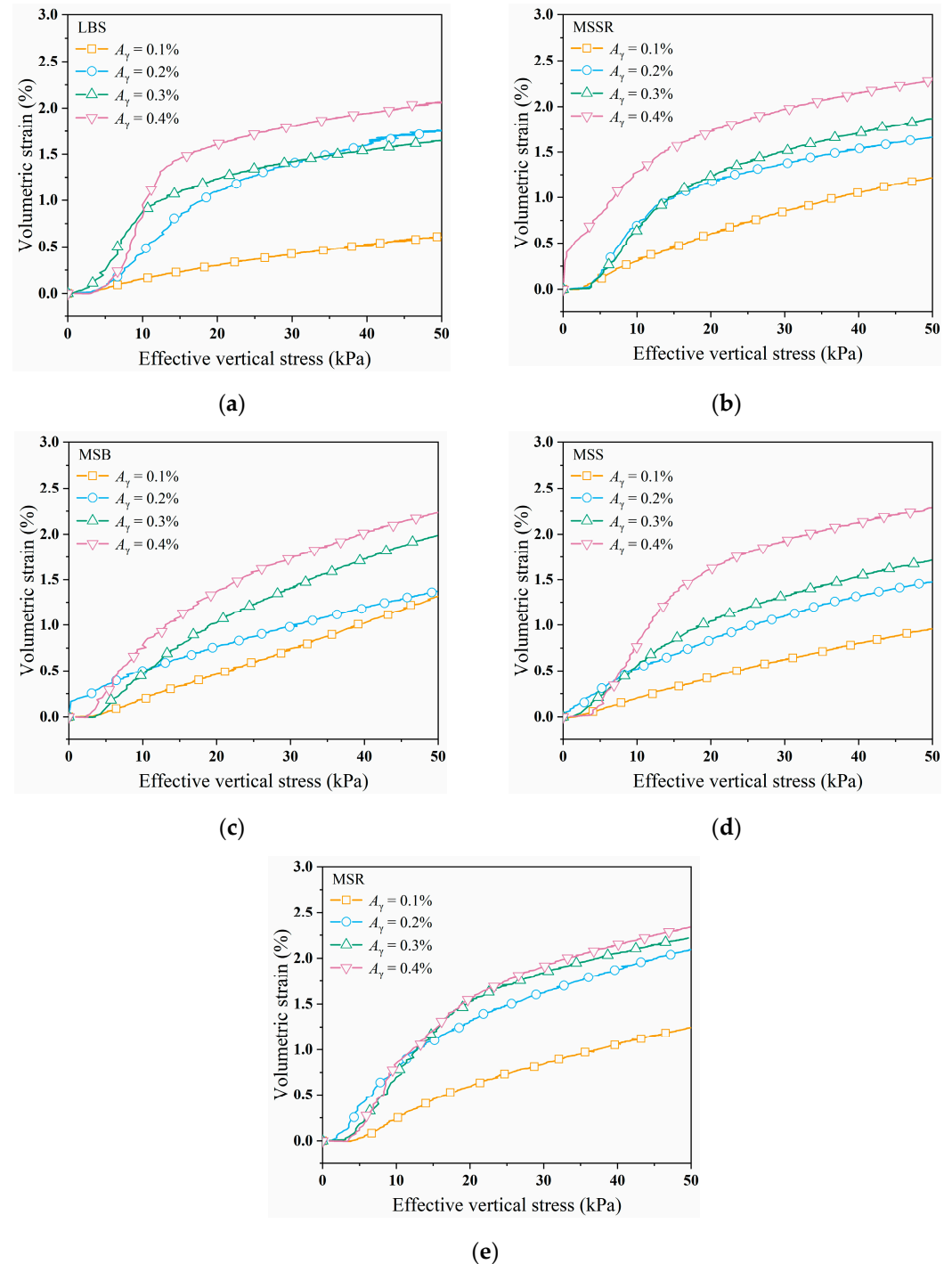
Figure 13. Volumetric strain development of re-consolidated samples with different shear histories: (**a**) LBS; (**b**) MSSR; (**c**) MSB; (**d**) MSS; and (**e**) MSR.

The stress-strain behaviors of the monotonic shear tests in the post-liquefaction stage are presented in Figure 14, while the results of the virgin samples that did not undergo cyclic shearing ($A_\gamma = 0$) serve as a reference. Compared with the samples that did not go through liquefaction, the shear strength of the post-liquefaction samples was enhanced after the cyclic shearing and re-consolidation. The peak shear stress before the shear strain

of 1% and the overall maximum shear stress of the MS samples were higher than that of the LBS sample during the post-liquefaction stage with a higher regularity under the same condition. For a specified regularity, the results showed that samples have higher shear strength if they had undergone larger shear strain amplitudes with the same cyclic number. This is because larger vibrations have caused greater rotation and slipping of particles, leading to larger volumetric strains in the re-consolidation stage and increasing the density of the samples. Under the coupling effect of the higher density and the particle shape, the internal structure became more stable and more difficult to slide over particles.
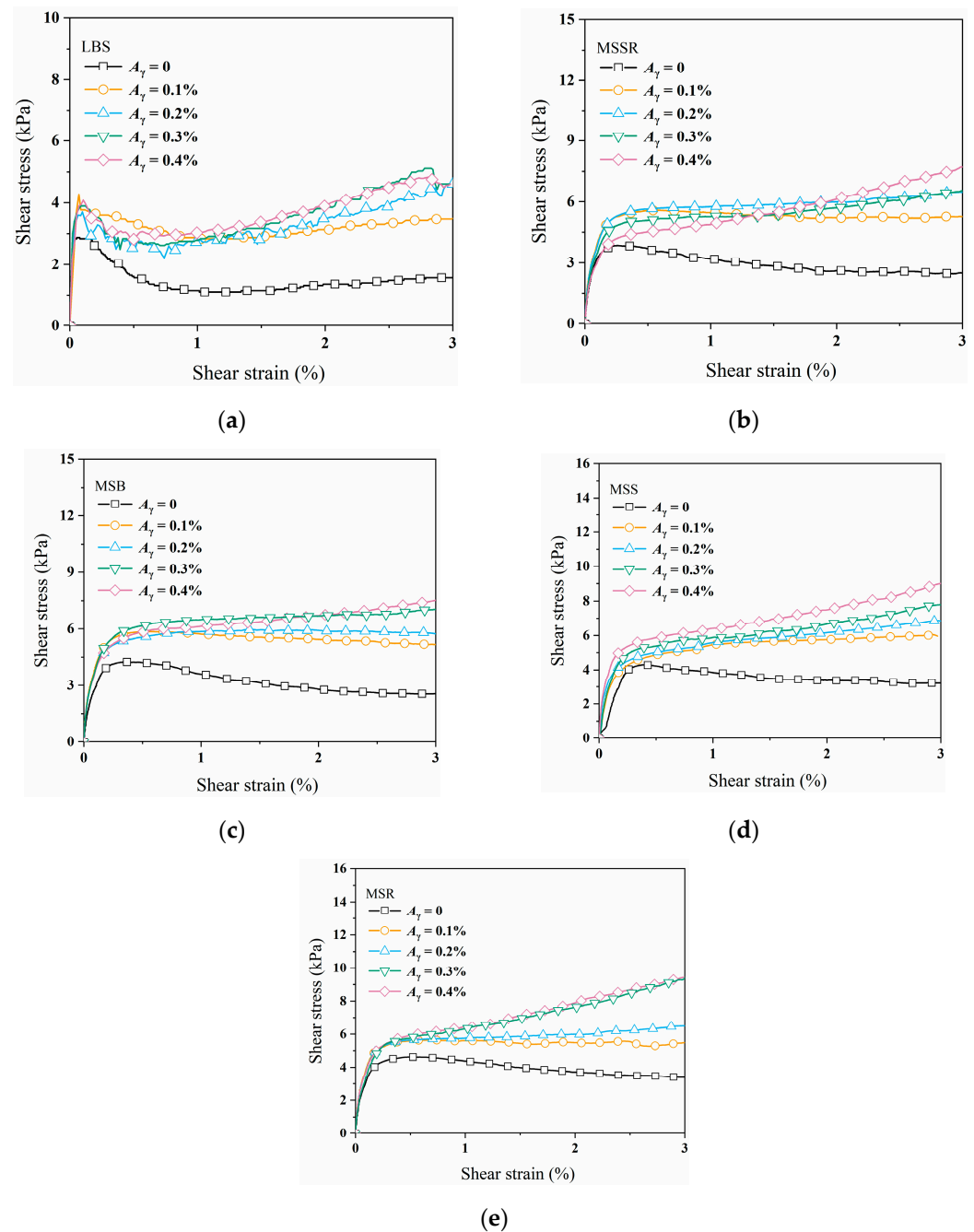
Figure 14. Shear stress-strain behaviors in PMS tests of samples with different shear amplitudes: (**a**) LBS; (**b**) MSSR; (**c**) MSB; (**d**) MSS; and (**e**) MSR.

4.2.1. Effects of Particle Shape on Maximum Shear Stress under Various Cyclic Shear Histories

In the post-liquefaction stage, a linear relationship was found when the maximum shear stress was compared with different shear strain amplitudes of the samples, as presented in Figure 15. The linear correction between the maximum shear stress and shear amplitude for different samples can be described by Equation (7):

$$\tau_{max-post} = K_\tau \cdot A_\gamma + I_\tau \tag{7}$$

where K_τ is the adjustment coefficient for maximum shear stress and I_τ is a basic parameter.
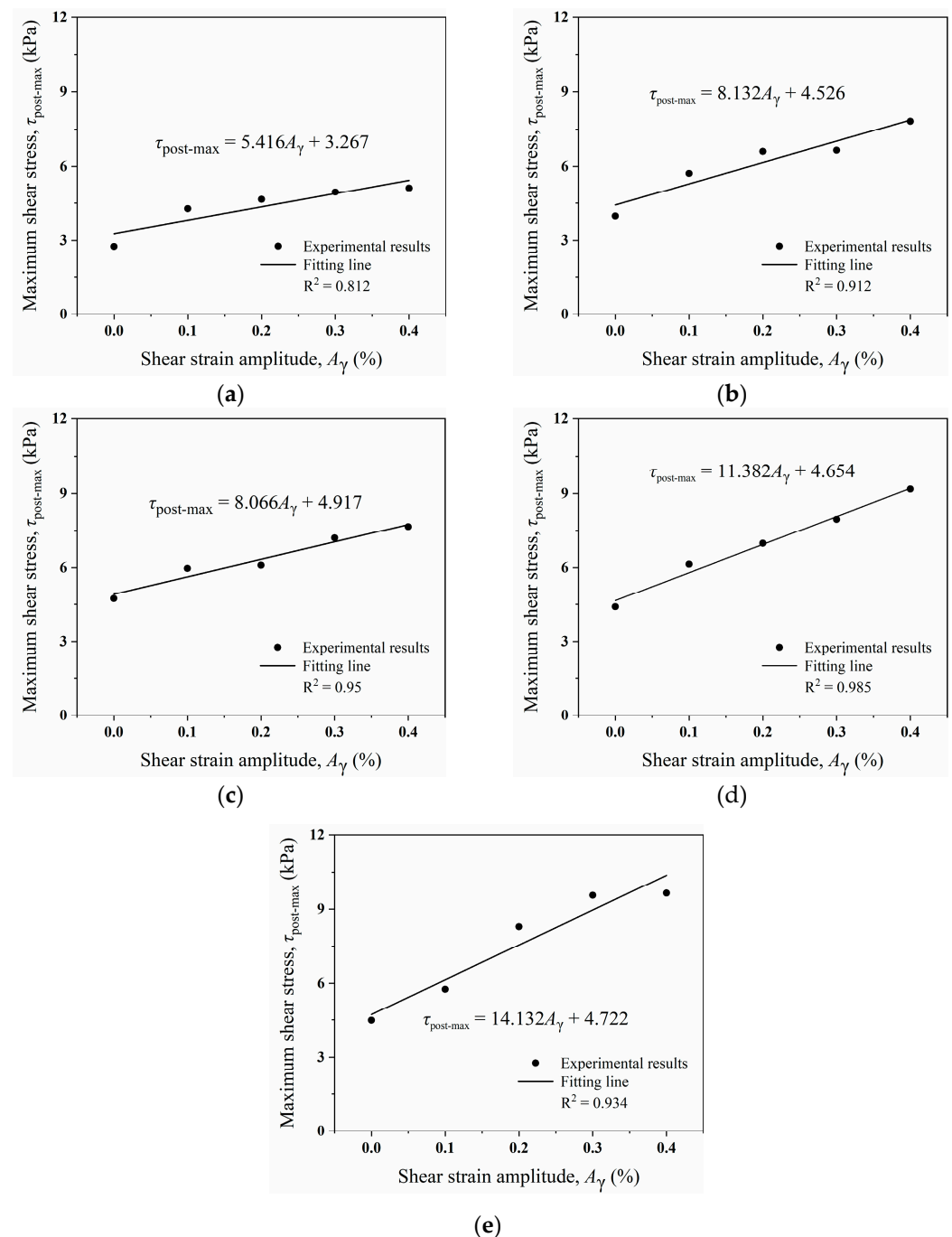
Figure 15. Relationship between the maximum shear stress and cyclic shear history of different samples: (**a**) LBS; (**b**) MSSR; (**c**) MSB; (**d**) MSS; and (**e**) MSR.

The values of K_τ and I_τ changes among the samples with different particle regularity, as listed in Table 4. It can be seen that the fitting line was gentle for the sample with the largest particle regularity of 0.803, which had the minimum adjustment coefficient K_τ of 5.416, while the sample with the minimum particle regularity of 0.432 had the greatest adjustment coefficient K_τ of 14.132. The results showed that the decrease of the particle regularity would lead to an increase of K_τ and shear strength in the PMS tests. In addition, the change of the shear strain amplitude and particle regularity did not seem to influence the intercept of the linear relationship, while the slope could be influenced considerably by the variation of particle regularity ρ.

Table 4. Values of K_τ and I_τ varying with particle regularity.

Material	Particle Regularity (ρ)	K_τ	I_τ
LBS	0.803	5.416	3.267
MSSR	0.607	8.132	4.526
MSB	0.536	8.066	4.917
MSS	0.498	11.382	4.654
MSR	0.432	14.132	4.722

4.2.2. Influences of Particle Shape and Shear History on the Pore Pressure

The pore pressure developments of the samples in Figure 16 show that during the post-liquefaction stage, the pore pressure of the samples generally reached a maximum value and decreased subsequently. The LBS sample shows the overall highest pore pressure under the same testing condition and the peak pore pressure of the LBS samples was found to be larger than that of the MS samples with the same cyclic shear amplitude A_γ. The results manifest that irregular particles of MS could effectively restrain the pore pressure generation. However, compared to the build-up of pore pressure in the pre-liquefaction stage, the liquefaction did not occur in this stage because the accumulation of pore pressure is induced by monotonic shear loading.

Meanwhile, the peak pore pressure was observed to decrease with the increased shear strain amplitude in the CSS tests. As the shear strain amplitude increased from 0.1% to 0.4%, the pore pressure of the LBS sample slightly decreased. This is because the higher shear amplitude led to larger volumetric strains in the re-consolidation phase and the density of samples was increased, which had a substantial impact on the subsequent pore pressure generation. For MS samples, the reduction of pore pressure was found more obvious with greater cyclic shear amplitude, which means that the MS samples with irregular particles are more sensitive to the cyclic shear history. The above results show the stability of the MS samples compared with LBS samples in the post-liquefaction stage and suggest that MS could serve as an appropriate substitution for quartz sand in foundation engineering under repeated cyclic loading conditions.

According to the experimental data, some correlations between the particle shape, shear strain amplitude, and pore pressure in the post-liquefaction phase are found. Figure 17 shows the influence of the particle shape and shear strain amplitude on the pore pressure. The particle shape and pore pressure were likewise shown to have a linear correlation. The slope remained relatively gentle, but the intercept dropped as the shear strain amplitude rose. The relationship is proposed as follows:

$$\mu_{max-post} = K_\mu \cdot \rho + E_A \cdot A_\gamma + I_\mu \tag{8}$$

where K_μ is the adjustment coefficient for the peak pore pressure, E_A is the scaling factor for shear strain amplitude A_γ, and I_μ is the state constant. In this study, the value of K_μ was taken as the average and the other parameters were derived by linear interpolation. The values of K_μ, E_A, and I_μ in this experiment were 30.096, -26.222, and 26.262, respectively.
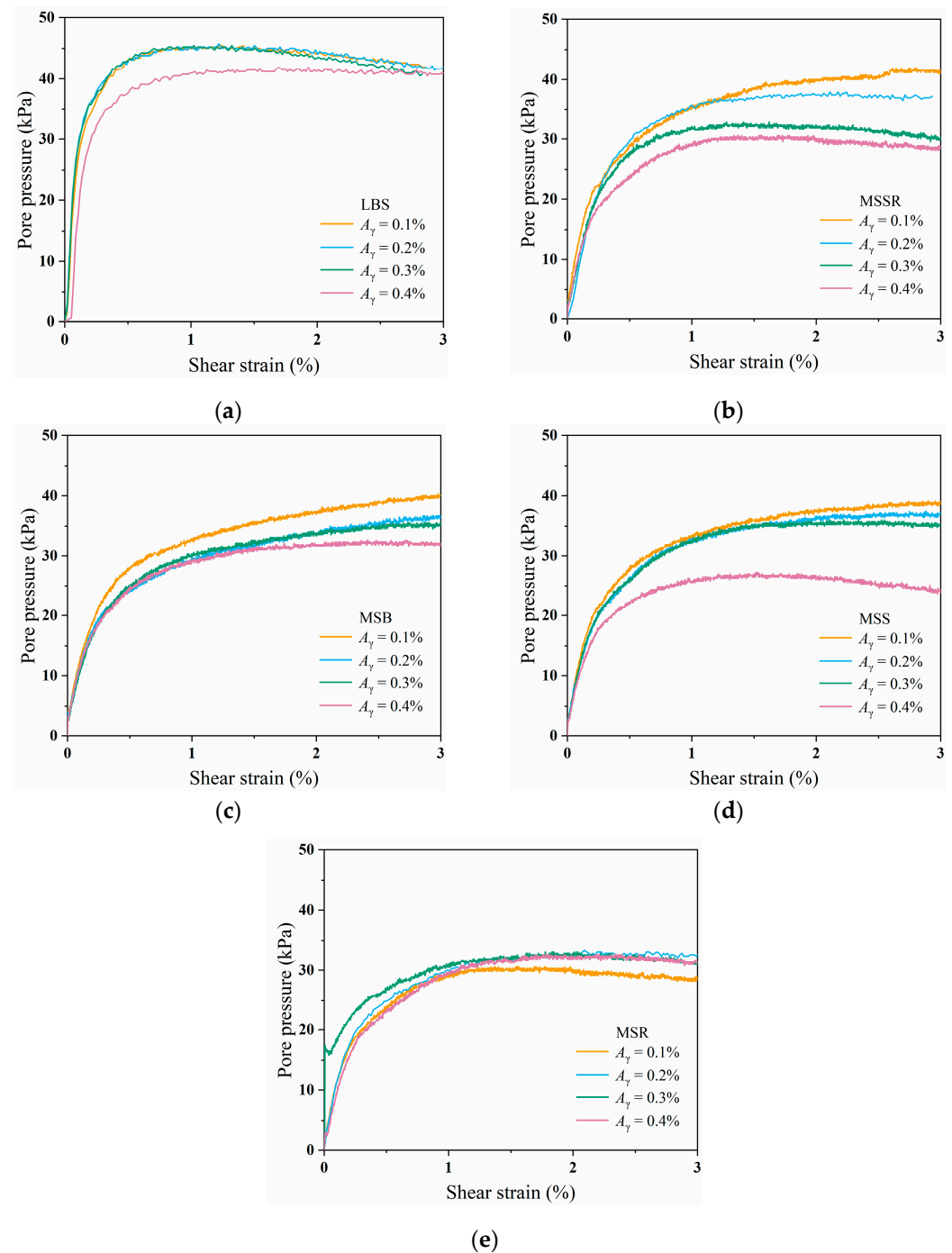
Figure 16. Pore pressure developments at the post-liquefaction stage of samples with different cyclic shear histories: (**a**) LBS; (**b**) MSSR; (**c**) MSB; (**d**) MSS; and (**e**) MSR.

In Figure 17, the linear regression fits these data well and predict the development of pore pressure. The prediction of the shear strength and pore pressure using the relationship could serve as a reference for numerical simulations and designs in engineering, for instance, to predict the pore pressure and shear strength in the seabed of reclamation which suffers from the monotonic shear stress of the nearby soil in the post-liquefaction stage after being subjected to a period of cyclic loadings.
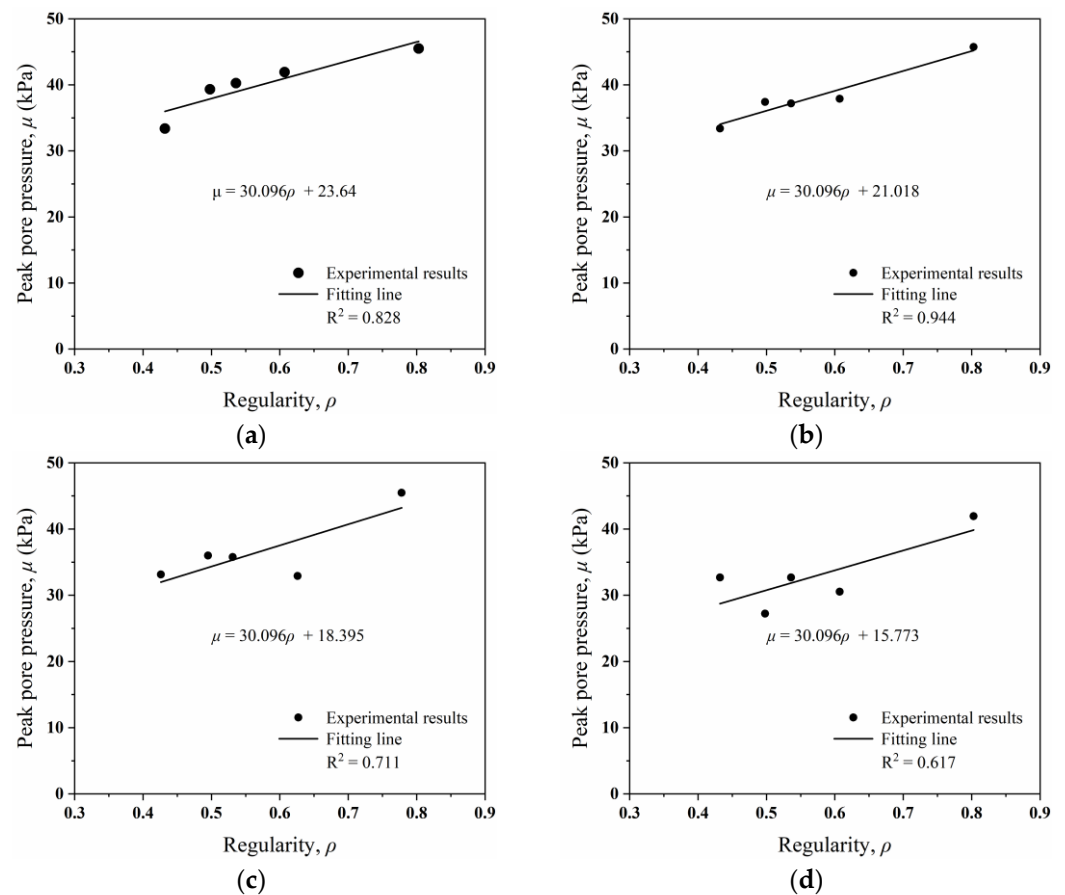
Figure 17. Relationships between the peak pore pressure and particle regularity with different cyclic shear histories: (**a**) $A_\gamma = 0.1\%$; (**b**) $A_\gamma = 0.2\%$; (**c**) $A_\gamma = 0.3\%$; and (**d**) $A_\gamma = 0.4\%$.

5. Conclusions

The coupling effect of the particle shape and cyclic shear history on different kinds of manufactured sand was investigated in this paper with a series of cyclic simple shear tests and post-liquefaction monotonic shear tests. The test results were compared and the relationships between different parameters of the regularity, friction angle, and shear performance of the samples were studied. Primary conclusions were found as follows:

1. It was found that irregular shapes not only increase the friction angles, but also enhance the shear stability of the MS samples. In the undrained CSS tests, the samples with irregular particles showed better shear performance and required more cycles to reach liquefaction. A power correlation between shear stiffness and loading cycles was proposed to describe the decrease in shear stiffness. For a given shear amplitude, particle regularity has a noticeable effect on the cyclic shear resistance as the irregular shapes strengthen the interlocking of particles and make them more difficult to dislocate, thus enhancing the cyclic shear resistance of MS.

2. In PMS tests, the samples that had undergone cyclic shearing were strengthened and their shear strength was higher than those that did not go through CSS tests. Moreover, the shear strength of the samples improved as the cyclic shear amplitude increased or the regularity of the particles decreased. The relationship between the shear amplitude and peak shear stress under monotonic shearing is proposed. Therefore, although the samples were tested in the same conditions, the MS samples had larger shear strength because the irregularity of the MS samples was generally higher than that of the LBS samples.

3. The pore pressure of the samples in the post-liquefaction phase reached the maximum value and then decreased gradually under the monotonic shear. The liner regression

between the peak pore pressure and particle regularity was established, which could serve as a reference for the prediction of the pore pressure and shear strength in geotechnical engineering.

4. The test results indicated that, generally, MS has a higher friction angle and better mechanical response compared with natural quartz sand. Therefore, MS could serve as the replacement of natural sand in backfilling projects. The relationships discovered in this paper between the shear performance and particle regularity could support the application and selection of MS in offshore and geotechnical engineering.

References

1. Celik, T.; Marar, K. Effects of crushed stone dust on some properties of concrete. *Cem. Concr. Res.* **1996**, *26*, 1121–1130. [CrossRef]
2. Bhoopathy, V.; Subramanian, S.S. The way forward to sustain environmental quality through sustainable sand mining and the use of manufactured sand as an alternative to natural sand. *Environ. Sci. Pollut. Res.* **2022**, *29*, 30793–30801. [CrossRef] [PubMed]
3. Skare, E.L.; Sheiati, S.; Cepuritis, R.; Mørtsell, E.; Smeplass, S.; Spangenberg, J.; Jacobsen, S. Rheology modelling of cement paste with manufactured sand and silica fume: Comparing suspension models with artificial neural network predictions. *Constr. Build. Mater.* **2022**, *317*, 126114. [CrossRef]
4. China Aggregates Association. Super Engineering. 1.1 Billion Tons of Sand and Stone Demand! The State Council Approved that the Expansion and Reclamation of Macao International Airport is Coming. Available online: https://www.sohu.com/a/602752180_99894134 (accessed on 15 January 2023).
5. China Aggregates Association. The Reclamation Project Costs more than 115 Billion Yuan and Uses about 250 Million to 300 Million Tons of Manufactured Sand and Construction Waste! This is just One of the Projects. Available online: http://www.zgss.org.cn/gongqiuxinxi/2021/12883.html (accessed on 15 January 2023).
6. Shen, W.; Yang, Z.; Cao, L.; Cao, L.; Liu, Y.; Yang, H.; Lu, Z.; Bai, J. Characterization of manufactured sand: Particle shape, surface texture and behavior in concrete. *Constr. Build. Mater.* **2016**, *114*, 595–601. [CrossRef]
7. Yang, J.; Yu, W.; Fang, H.Y.; Huang, X.Y.; Chen, S.J. Detection of size of manufactured sand particles based on digital image processing. *PLoS ONE* **2018**, *13*, e0206135. [CrossRef]
8. Yang, R.; Yu, R.; Shui, Z.; Guo, C.; Wu, S.; Gao, X.; Peng, S. The physical and chemical impact of manufactured sand as a partial replacement material in Ultra-High Performance Concrete (UHPC). *Cem. Concr. Compos.* **2019**, *99*, 203–213. [CrossRef]
9. Zhu, J.; Liu, J.; Khayat, K.H.; Shu, X.; Ran, Q.; Li, Z. Mechanisms affecting viscosity of cement paste made with microfines of manufactured sand. *Cem. Concr. Res.* **2022**, *156*, 106757. [CrossRef]
10. Altuhafi, F.; O'Sullivan, C.; Cavarretta, I. Analysis of an image-based method to quantify the size and shape of sand particles. *J. Geotech. Geoenvironmental Eng.* **2013**, *139*, 1290–1307. [CrossRef]
11. Yang, J.; Luo, X.D. Exploring the relationship between critical state and particle shape for granular materials. *J. Mech. Phys. Solids* **2015**, *84*, 196–213. [CrossRef]
12. de Bono, J.; McDowell, G. The effects of particle shape on the yielding behaviour of crushable sand. *Soils Found.* **2020**, *60*, 520–532. [CrossRef]
13. Seo, D.; Sohn, C.; Cil, M.B.; Buscarnera, G. Evolution of particle morphology and mode of fracture during the oedometric compression of sand. *Geotechnique* **2021**, *71*, 853–865. [CrossRef]
14. Yang, J.; Luo, X.D. The critical state friction angle of granular materials: Does it depend on grading? *Acta Geotech.* **2018**, *13*, 535–547. [CrossRef]
15. Yang, J.; Wei, L.M. Collapse of loose sand with the addition of fines: The role of particle shape. *Geotechnique* **2012**, *62*, 1111–1125. [CrossRef]
16. Maeda, K.; Sakai, H.; Kondo, A.; Yamaguchi, T.; Nukudani, E. Stress-chain based micromechanics of sand with grain shape effect. *Granul. Matter.* **2010**, *12*, 499–505. [CrossRef]

17. Altuhafi, F.N.; Coop, M.R.; Georgiannou, V.N. Effect of particle shape on the mechanical behavior of natural sands. *J. Geotech. Geoenvironmental Eng.* **2016**, *142*, 04016071. [CrossRef]

18. Seed, H.B.; Lee, K.L.; Idriss, I.M.; Makdisi, F.I. The slides in the San Fernando dams during the earthquake of February 9, 1971. *J. Geotech. Eng. Div.* **1975**, *101*, 651–688. [CrossRef]

19. Shamoto, Y.; Zhang, J.-M.; Goto, S. Mechanism of large post-liquefaction deformation in saturated sand. *Soils Found.* **1997**, *37*, 71–80. [CrossRef]

20. Aguirre, J.; Irikura, K. Nonlinearity, liquefaction, and velocity variation of soft soil layers in Port Island, Kobe, during the Hyogo-ken Nanbu earthquake. *Bull. Seismol. Soc. Am.* **1997**, *87*, 1244–1258. [CrossRef]

21. Kokusho, T.; Hara, T.; Hiraoka, R. Undrained shear strength of granular soils with different particle gradations. *J. Geotech. Geoenvironmental Eng.* **2004**, *130*, 621–629. [CrossRef]

22. Sato, K.; Kokusho, T.; Matsumoto, M.; Yamada, E. Nonlinear seismic response and soil property during strong motion. *Soils Found.* **1996**, *36*, 41–52. [CrossRef]

23. Rabeti Moghadam, M.; Alielahi, H.; Sadeghi Abdollahi, A. Numerical evaluation of liquefaction-induced damages in composite breakwaters and its application for performance-based improvement design. *Mar. Georesources Geotechnol.* **2017**, *35*, 376–396. [CrossRef]

24. Hu, A.F.; Fu, P.; Xia, C.Q.; Xie, K.H. Lateral dynamic response of a partially embedded pile subjected to combined loads in saturated soil. *Mar. Georesources Geotechnol.* **2017**, *35*, 788–798. [CrossRef]

25. Hachey, J.; Been, K.; Jefferies, M.G. The critical state of sands. *Geotechnique* **1991**, *41*, 365–381.

26. Silver, M.L.; Bolton, S.H. Volume Changes in Sands during Cyclic Loading. *J. Soil Mech. Found. Div.* **1971**, *97*, 1171–1182. [CrossRef]

27. Leslie, Y.T. Compaction of Sands by Repeated Shear Straining. *J. Soil Mech. Found. Div.* **1972**, *98*, 709–725.

28. Polito, C.P.; Martin, J.R., II. Effects of nonplastic fines on the liquefaction resistance of sands. *J. Geotech. Geoenvironmental Eng.* **2001**, *127*, 408–415. [CrossRef]

29. Shamoto, Y.; Zhang, J.-M. Evaluation of Seismic Settlement Potential of Saturated Sandy Ground Based On Concept of Relative Compression. *Soils Found.* **1998**, *38*, 57–68. [CrossRef]

30. Zhang, H.; Yang, Y.; Yu, H.S. Liquefaction and post-liquefaction of granular material under multi-directional cyclic loading. *Mar. Georesources Geotechnol.* **2021**, *39*, 1261–1272. [CrossRef]

31. Ahn, I.S.; Cheng, L. Tire derived aggregate for retaining wall backfill under earthquake loading. *Constr. Build. Mater.* **2014**, *57*, 105–116. [CrossRef]

32. Moghaddas Tafreshi, S.N.; Norouzi, A.H. Bearing capacity of a square model footing on sand reinforced with shredded tire - An experimental investigation. *Constr. Build. Mater.* **2012**, *35*, 547–556. [CrossRef]

33. Shariatmadari, N.; Norouzi, M.; Rezvani, R. Stress–strain behavior of marine calcareous soil-tire mixtures. *Mar. Georesources Geotechnol.* **2021**, *40*, 739–750. [CrossRef]

34. McKelvey, D.; Sivakumar, V.; Bell, A.; McLaverty, G. Shear strength of recycled construction materials intended for use in vibro ground improvement. *Ground Improv.* **2002**, *6*, 59–68. [CrossRef]

35. Li, B.; Wang, Y.; Jin, Q.; Chen, H. Liquefaction characteristics of recycled concrete aggregates. *Soil Dyn. Earthq. Eng.* **2019**, *120*, 85–96. [CrossRef]

36. Herrador, R.; Pérez, P.; Garach, L.; Ordóñez, J. Use of Recycled Construction and Demolition Waste Aggregate for Road Course Surfacing. *J. Transp. Eng.* **2011**, *138*, 182–190. [CrossRef]

37. Huang, Y.; Wang, J.; Ying, M.; Ni, J.; Li, M. Effect of particle-size gradation on cyclic shear properties of recycled concrete aggregate. *Constr. Build. Mater.* **2021**, *301*, 124143. [CrossRef]

38. Jiménez, J.R.; Ayuso, J.; Agrela, F.; López, M.; Galvín, A.P. Utilisation of unbound recycled aggregates from selected CDW in unpaved rural roads. *Resour. Conserv. Recycl.* **2012**, *58*, 88–97. [CrossRef]

39. Maduabuchukwu Nwakaire, C.; Poh Yap, S.; Chuen Onn, C.; Wah Yuen, C.; Adebayo Ibrahim, H. Utilisation of recycled concrete aggregates for sustainable highway pavement applications: A review. *Constr. Build. Mater.* **2020**, *235*, 117444. [CrossRef]

40. Saberian, M.; Li, J.; Nguyen, B.; Wang, G. Permanent deformation behaviour of pavement base and subbase containing recycle concrete aggregate, coarse and fine crumb rubber. *Constr. Build. Mater.* **2018**, *178*, 51–58. [CrossRef]

41. *ASTM D4253*; Standard Test Methods for Maximum Index Density and Unit Weight of Soils Using a Vibratory Table. ASTM International: West Conshohocken, PA, USA, 2016.

42. *ASTM D4254*; Standard Test Method for Minimum Index Density and Unit Weight of Soils and Calculation of Relative Density. ASTM International: West Conshohocken, PA, USA, 2016.

43. Wadell, H. Volume, Shape, and Roundness of Rock Particles. *J. Geol.* **1932**, *40*, 443–451. [CrossRef]

44. Krumbein, W.C. Measurement and Geological Significance of Shape and Roundness of Sedimentary Particles. *SEPM J. Sediment. Res.* **1941**, *11*, 64–72. [CrossRef]

45. Cho, G.C.; Dodds, J.; Santamarina, J.C. Closure to "Particle shape effects on packing density, stiffness, and strength: Natural and crushed sands" by Gye-Chun Cho, Jake Dodds, and J. Carlos Santamarina. *J. Geotech. Geoenvironmental Eng.* **2007**, *133*, 1474. [CrossRef]

46. Suh, H.S.; Kim, K.Y.; Lee, J.; Yun, T.S. Quantification of bulk form and angularity of particle with correlation of shear strength and packing density in sands. *Eng. Geol.* **2017**, *220*, 256–265. [CrossRef]

47. Xiao, Y.; Long, L.; Evans, T.M.; Zhou, H.; Liu, H.; Stuedlein, A.W. Effect of particle shape on stress-dilatancy responses of medium-dense sands. *J. Geotech. Geoenvironmental Eng.* **2019**, *145*, 04018105. [CrossRef]

48. He, Z.; Shen, A.; Wu, H.; Wang, W.; Wang, L.; Guo, Y. Properties and mechanisms of brick-concrete recycled aggregate strengthened by compound modification treatment. *Constr. Build. Mater.* **2022**, *315*, 125678. [CrossRef]

49. Ying, M.; Liu, F.; Wang, J.; Wang, C.; Li, M. Coupling effects of particle shape and cyclic shear history on shear properties of coarse-grained soil–geogrid interface. *Transp. Geotech.* **2021**, *27*, 100504. [CrossRef]

50. Zheng, J.; Hryciw, R.D. Traditional soil particle sphericity, roundness and surface roughness by computational geometry. *Geotechnique* **2015**, *65*, 494–506. [CrossRef]

51. Zheng, J.; Hryciw, R.D. Index void ratios of sands from their intrinsic properties. *J. Geotech. Geoenvironmental Eng.* **2016**, *142*, 06016019. [CrossRef]

52. *ASTM D8296-19*; Standard Test Method for Consolidated Undrained Cyclic Direct Simple Shear Test under Constant Volume with Load Control or Displacement Control. ASTM International: West Conshohocken, PA, USA, 2019.

53. Chiaro, G.; Koseki, J.; Sato, T. Effects of initial static shear on liquefaction and large deformation properties of loose saturated Toyoura sand in undrained cyclic torsional shear tests. *Soils Found.* **2012**, *52*, 498–510. [CrossRef]

54. Della, N.; Belkhatir, M.; Arab, A.; Canou, J.; Dupla, J.C. Undrained Monotonic Response and Instability of Medium-Dense Sandy Soil. *Mar. Georesources Geotechnol.* **2015**, *33*, 487–495. [CrossRef]

55. Wang, Y.; Gao, Y.; Guo, L.; Cai, Y.; Li, B.; Qiu, Y.; Mahfouz, A.H. Cyclic response of natural soft marine clay under principal stress rotation as induced by wave loads. *Ocean. Eng.* **2017**, *129*, 191–202. [CrossRef]

56. Dyvik, R.; Berre, T.; Lacasse, S.; Raadim, B. Comparison of truly undrained and constant volume direct simple shear tests. *Geotechnique* **1987**, *37*, 3–10. [CrossRef]

57. Wang, Z.; Yang, Y.; Li, Y.; Liu, S.; Zhou, P. Numerical simulation of cyclic shear tests considering the fabric change and principal stress rotation effects. *Int. J. Numer. Anal. Methods Geomech.* **2022**, *46*, 1409–1432. [CrossRef]

58. Keramatikerman, M.; Chegenizadeh, A. Effect of Particle Shape on Monotonic Liquefaction: Natural and Crushed Sand. *Exp. Mech.* **2017**, *57*, 1341–1348. [CrossRef]

59. Rui, S.; Guo, Z.; Si, T.; Li, Y. Effect of particle shape on the liquefaction resistance of calcareous sands. *Soil Dyn. Earthq. Eng.* **2020**, *137*, 106302. [CrossRef]